Self-assembly of complex structures in colloid-polymer mixtures

Erdal C. Oğuz*
School of Mechanical Engineering and The Sackler Center for Computational Molecular and Materials Science, Tel Aviv University, Tel Aviv 6997801, Israel

Aleksandar Mijailović
Institut für Theoretische Physik II, Heinrich-Heine Universität, Universitätsstr. 1, 40225 Düsseldorf, Germany and Institut für Theoretische Physik 1, Friedrich-Alexander-Universität Erlangen-Nürnberg, Staudtstrasse 7, 91058 Erlangen, Germany

Michael Schmiedeberg
Institut für Theoretische Physik 1, Friedrich-Alexander-Universität Erlangen-Nürnberg, Staudtstrasse 7, 91058 Erlangen, Germany

(Received 15 March 2017; published 2 November 2018)

If particles interact according to isotropic pair potentials that favor multiple length scales, in principle, a large variety of different complex structures can be achieved by self-assembly. Here, we study the specific example of colloid-polymer mixtures in which the effective interactions between colloids are dictated by a Aasakura-Osawa–type potential that possesses two length scales. Upon examining the phase behavior of two-dimensional colloid-polymer mixtures, we observe that nontrivial structures only occur in the vicinity of selected densities where triangular ordering is suppressed by the pair potential. Close to these densities, a large number of different phases self-assemble that correspond to tilings containing triangular, rhombic, square, hexagonal, and pentagonal tiles, and including some of the Archimedean tilings. We obtain the ground-state energies by minimizing the corresponding lattice sums with respect to particle positions in a unit cell as well as cell geometry and verify the occurrence of selected phases at finite temperatures by using Brownian dynamics simulations. We explain how the occurrence of nontrivial orderings can be predicted on a two-particle level by employing an enthalpylike pair potentials. Our work provides a manual on how to find the regions of nontrivial phases in parameter space for complex pair interactions in general.

DOI: 10.1103/PhysRevE.98.052601

I. INTRODUCTION

Self-assembly is the process by which the system constituents form large organized functional units via their mutual interactions without any external influence. Since the pioneering work by Whitesides *et al.* [1] on molecular systems, self-assembly has been studied in great detail in a wide range of length scales ranging from atomic to macroscopic systems and throughout various scientific disciplines, including physics, chemistry, materials science, and biology [2–14].

In monodisperse systems that do not possess more than one characteristic length scale self-assembly usually occurs in the same way as for hard disks or spheres, i.e., the particles form a triangular phase in two or a fcc-crystal in three dimensions and at appropriate conditions. Beyond such simple systems, a plethora of self-assembled complex structures can be achieved in mixtures of different particle types such as in metallic alloys [15] or in binary colloidal suspensions [16–18]. Two further scenarios pave the way for high structural complexity in one-component systems by requiring (i) an interaction or shape anisotropy and (ii) a deliberate choice of an isotropic pair interaction with multiple length scales that affect the structure formation. Prototypical examples of the former are hard convex polyhedra packings [19] and patchy colloids [20–22], whereas concerning the latter inverse statistical-mechanical approaches have been undertaken to investigate the self-assembly of nontriangular ground-state structures with engineered pair interaction potentials [23–26]. More recently it has even been shown that complex ground-state structures can be stabilized by repulsive and convex pair interaction potentials which rule out the necessity for single- or multiple wells in this potential [27–32]. Note that in general determining the phase behavior from just the pair potential in nontrivial [33].

A system that is well-studied in theory and simulation and in addition can be realized and investigated experimentally is a charge-stabilized colloid-polymer mixture which intrinsically involves multiple length scales as the colloids effectively attract each other close to contact due to depletion interactions while being repulsive on larger length scales because of screened electrostatic repulsions. Experimental and theoretical studies have been performed to understand the nature of colloid-polymer mixtures [34–45] some of which exhibit glassy states [37,38], gels [39–43], and cluster formation [42,44,45]. The phase behavior concerning the gas, liquid, and trivial solid phase has been investigated in Refs. [46–57]. Moreover, the influence of many-body interactions on the phase behavior of such mixtures [58,59] as well as confinement effects [60–63] have been analyzed recently. However,

*erdaloguz@mail.tau.ac.il

to the best of our knowledge, detailed structural analysis of the crystal phase were not in the focus of previous studies, nor any nontrivial complex ordering have been reported with the exception of local ground-state clusters [42,45].

In this article, we determine the ground states that occur in a colloid-polymer mixture in two dimensions. The ground-state orderings are calculated by minimizing the energy for structures with one to six particles per unit cell. Aside from the trivial triangular phase, we observe square, rhombic, triangular, honeycomb, Kagome, and Archimedean tilings [64–67] as well as further orderings that correspond to tilings with hexagons and even pentagons. We further run Brownian dynamics computer simulations to verify the existence of occurring phases at finite temperatures.

To understand why nontrivial structures in monodisperse systems with isotropic interactions can occur in general, we determine the enthalpy on a two-particle level and demonstrate that the resulting enthalpy-like pair potential can be used to identify the parameters where triangular structures are suppressed. Our approach explains why and how even monotonic pair potentials can be used to self-assemble complex phases.

The article is structured as follows: We introduce the system and methods in Sec. II. In Sec. III we first comment on the comparison of results in the ground state and results at finite temperature. Then, we discuss the observed phases in detail before we explain the enthalpy-like pair potential that can be used to predict the occurrence of nontrivial phases. Finally, we conclude in Sec. IV.

II. SYSTEM AND METHODS

A. Colloid-polymer mixtures

When immersed in a solvent of relatively small-sized non-adsorbing polymer coils, the larger colloidal particles sense a short-ranged *depletion* attraction at sufficiently high polymer concentrations. This attractive force arises due to an unbalanced osmotic pressure stemming from the depletion zone in the region between the colloids.

The effective pair interaction potential between the center points of the colloids in the presence of the polymers is given by a screened Coulomb repulsion corresponding to a Yukawa-like interaction, and on short lengths by depletion attraction where we employ the AO-model [68,69]. Since polymers can only enter the gap between two colloids if this gap is wider than the size of the colloids, in the AO-approach one considers an effective attraction due to the resulting depletion that is proportional to the area that cannot be accessed by polymers. Therefore, the pair interaction potential is [68,69]

$$v(r_{ij}) = \begin{cases} V_0 \frac{\exp(-\kappa r_{ij})}{\kappa r_{ij}} - W_0\left[1 - \frac{3r_{ij}}{2d} + \frac{r_{ij}^3}{2d^3}\right] & \text{if } r_{ij} \leqslant d, \\ V_0 \frac{\exp(-\kappa r_{ij})}{\kappa r_{ij}} & \text{if } r_{ij} > d, \end{cases} \tag{1}$$

where r_{ij} is the separation distance between colloids i and j, κ denotes the inverse screening length, and d the length that is given by the depletion effect. To be specific, this depletion length d corresponds to the sum of the effective diameter of a colloid plus the effective diameter of a polymer. Note that for our calculations we do not have to consider any hard core colloid-colloid interactions, because in the ground state such an hard core repulsion would only matter if two particles touched. Therefore, our ground state results are valid for all colloidal hard core diameters that are smaller or equal than the smallest distance between two colloids. The energy amplitude of the pure electrostatic Yukawa interaction is given by V_0, whereas the strength of the depletion potential is set by W_0. The crystalline phase diagrams can therefore be determined in three-dimensional space spanned by the reduced energy amplitude V_0/W_0, the reduced density $\sqrt{\rho}d$, and the reduced depletion length κd corresponding to the ratio of depletion length divided by screening length.

We primarily explore the ground state of our model colloid-polymer mixtures by determining the corresponding phase diagrams in the $(\sqrt{\rho}d, \kappa d)$-plane at fixed V_0/W_0. At zero temperature, the optimal structures with N particles are those that minimize the total internal energy,

$$U = \frac{1}{2}\sum_{\substack{i,\,j \\ i\neq j}}^{N} v(r_{ij}), \tag{2}$$

at a given reduced density, depletion length, and energy amplitude. We use a direct lattice summation technique to determine U, and thus to predict the corresponding ground-state structures. To examine the stability of resulting structures at finite temperatures, we extend our studies to $T > 0$ by means of Brownian dynamics computer simulations. In the following, we provide details for both the lattice summation and the finite-temperature simulations used in this work.

B. Lattice-sum calculations

At each given density $\sqrt{\rho}d$, depletion length κd, and energy amplitude V_0/W_0, we have performed lattice sum minimizations for a set of candidates of crystalline lattices. As possible candidates, we consider two-dimensional crystals with a periodicity in both the spatial directions x and y whose primitive cell is a parallelogram containing n particles, see Appendix A. We consider candidates with primitive cells comprising up to 6 particles, i.e., $n = 1, \cdots, 6$, with no further restrictions.

At prescribed parameters, the total potential energy per particle $u = U/N$ [cf. Eq. (2)] is minimized with respect to the particle coordinates of the basis, and the cell geometry. To be specific, we implement the Nelder-Mead method (also known as downhill simplex method or amoeba method) to find the minimum of the energy functions [70]. As this technique is a heuristic approach, and thus it may not always converge to the global minimum, we use at least 200 and at most 1000 different start configurations depending on the complexity of those functions. Details are provided in Appendix A.

C. Brownian dynamics computer simulations

To study the validity of our theoretical ground-state predictions at finite but relatively low temperatures, we employ Brownian dynamics computer simulations in the NVT-ensemble by solving the Langevin equation for an overdamped system. The position $\mathbf{r}_i$ of particle i undergoing

Brownian motion after a time step δt is

$$\mathbf{r}_i(t+\delta t) = \mathbf{r}_i(t) + \frac{D}{k_B T}\mathbf{F}_i(t)\delta t + \delta \mathbf{W}_i, \tag{3}$$

where D denotes the free diffusion coefficient, $k_B T$ the thermal energy, and $\mathbf{F}_i$ is the total conservative force acting on particle i and stemming from the pair interaction v in Eq. (1). The random displacement $\delta \mathbf{W}_i$ is sampled from a Gaussian distribution with zero mean and variance $2D\delta t$ (for each Cartesian component) fixed by the fluctuation-dissipation relation. The time step is chosen as $\delta t = 10^{-5}\tau$, where $\tau = 1/(\kappa^2 D_0)$ is used as the unit of the time. We run simulations for up to $10^5\tau$, starting from a random distribution, a triangular or a square lattice of $N = 2000$ particles in a rectangular simulation box under periodic boundary conditions. All three runs yield the same final configurations at predetermined density and depletion length, suggesting the thermodynamical stability of our results rather than possible metastable configurations.

It is noteworthy that more sophisticated simulation algorithms making use of nonrectangular simulation boxes [71] might yield stable phases which we are not able to capture here in our simulations. This being said, however, we do not expect a radical change in the morphology of the phase diagram. In soft systems, the coexistence between two main phases will most likely suppress the occurrence of subtle phases with free-energies relatively close to each other and to the aforementioned main phases. Moreover, we want to emphasize that our main goal lies in determining the ground state of colloid-polymer mixtures, where we consider nonrectangular boxes, and comparing the results to the predictions of our enthalpy-based theory, where simulations shall only serve as an additional supportive data to strengthen our findings.

In the following, we present the results from both the zero-temperature lattice-sum minimizations and the finite-temperature simulations.

III. RESULTS

Before delving into the ground-state phase diagram for the given example of colloid-polymer mixtures in detail, i.e., determining each single phase structure at prescribed density and depletion length, we first report on the occurrence of nontriangular phases in coarse-grained phase diagrams both at zero- and finite temperature.

A. Zero- and finite-temperature phase diagrams

In Fig. 1 we show the phase diagrams of a model colloid-polymer mixture as a function of reduced density $\sqrt{\rho}d$ and reduced depletion length κd. The nontriangular crystalline phases only occur in special parameter regions. These regions are marked in Fig. 1 in yellow for ground states as determined by minimizing the interaction energy. We have further investigated the stability of nontriangular phases at finite temperatures by means of Brownian dynamics computer simulations. Particularly, we consider a temperature such that $V_0/k_B T = 1000$ and we fix the energy amplitudes to $V_0/W_0 = 1$. We reveal the stability of nontriangular crystals in the blue regions shown in Fig. 1. The similarity to the

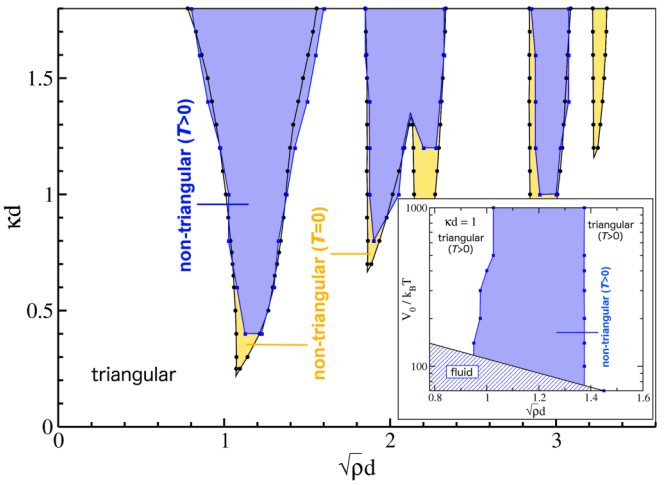

FIG. 1. Zero- and finite-temperature phase diagrams of colloid-polymer mixtures as a function of the reduced density $\sqrt{\rho}d$ and the reduced depletion length κd. The nontriangular stability modes as determined by lattice-sum minimizations and Brownian dynamics simulations are shown by yellow (at $T = 0$) and blue (at $T > 0$) regions, respectively. The actual determined phase points at the boundary are indicated by black dots and blue squares. The inset shows the solid- and fluid-state phase diagram as a function of the reduced density and the reduced inverse temperature at fixed $\kappa d = 1$. Details are explained in the text.

nontriangular stability regimes at $T = 0$ (shown in yellow in Fig. 1) is striking. Specifically, in both cases, the majority of the parameter space in the $(\sqrt{\rho}d, \kappa d)$ plane is governed by the triangular crystal as shown by the white region in Fig. 1. Nontriangular phases only occur in the vicinity of specific densities and for sufficiently large values of κd.

Moreover, the inset of Fig. 1 provides the evolution of the nontriangular solid phase space at $\kappa d = 1$ as a function of the inverse reduced temperature where melting is observed upon rising the temperature. Note also that at finite temperatures, the system melts as $\sqrt{\rho}d \to 0$. The melting is, however, out of the scope of this paper, and therefore not analyzed further here.

The phase diagrams in Fig. 1 have been determined at a finite ratio of the energy scales, $W_0/V_0 = 1$. Note that in the limit $W_0 \to 0$ the only solid phase in two dimensions possesses triangular order while in three dimensions in principle transitions between different solid states might occur [72,73].

Note that with the simulations we observe typical examples out of almost all of the different occurring phase categories as listed and explained in the next subsection. As the main goal of this manuscript is to provide a detailed view of self-assembly of complex phases at $T = 0$, simulations are only supposed to serve as additional data to strengthen the ground-state results. Therefore, we content ourselves to show some characteristic simulation snapshots for the occurring phases rather than describing the finite-temperature phase diagram thoroughly.

B. Detailed phase diagram of a colloid-polymer mixture

In the following, we explore the ground-state phase diagram of a colloid-polymer mixture in detail. The stability

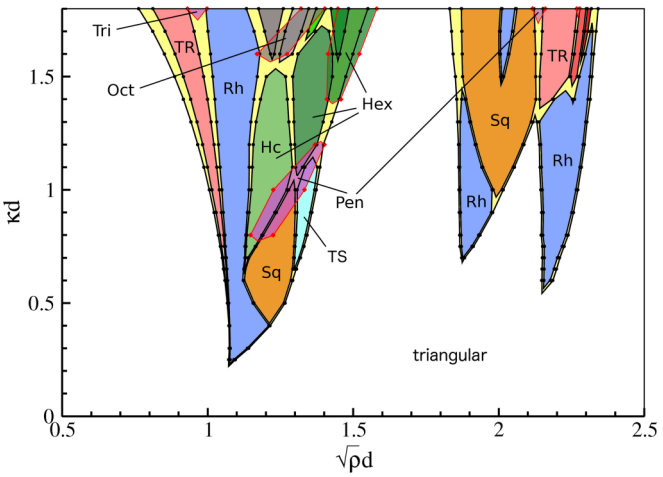

FIG. 2. Detailed zero-temperature phase diagram of a colloid-polymer mixture as a function of the reduced density $\sqrt{\rho}d$ and the reduced depletion length κd. The large white zone indicates the stability of the triangular phase, whereas other colors have been used to demonstrate the nontriangular stability regimes that include a variety of phase structures, each colored differently and labeled as follows: Sq, square phase; Rh, rhombic phase; Hex, hexagon-based structures including the honeycomb (Hc) lattice; Oct, octagon-based structures; Tri, trimers; TR, triangle-rectangular structures; TS, triangle-square structures; Pen, pentagon-based structures. The black dots are the actual computed phase points at the boundary of nontriangular phases. The yellow areas illustrate the coexistence between the neighboring phases. The phases are shown for up to 4 particles per unit cell. The regions where we find additional phases with five or six particles per unit cell are marked by transparent colors. While outside of these regions we do not expect the occurrence of phases with even more particles per unit cell, within the transparent regions more complex phases might be stable.

of zero-temperature crystalline phases are shown in Fig. 2 for $\sqrt{\rho}d \leqslant 2.5$ and $\kappa d \leqslant 1.8$. In Fig. 2 we show the detailed phase behavior for the first nontriangular regions with lowest density. The phase diagram reveals a large structural diversity. The white region indicates the stability regime of the triangular lattice as before, whereas the colored areas demonstrate the occurrence of stable nontriangular phases of different symmetry and complexity. Here, we obtain simple phases with $n = 1$ particle per unit cell such as rhombic (Rh) and square (Sq) lattices as shown by blue and orange regions in Fig. 2 as well as more complex structures with $n \geqslant 2$. The latter possess a richer diversity and can be grouped into hexagon-based (Hex, green regions) structures including the honeycomb (Hc) lattice, octagon-based (Oct, gray regions) structures, trimers (Tri, purple), triangle-rectangular (TR, red regions), and triangle-square (TS, turquoise region) structures, and finally the pentagon-based (Pen, purple transparent regions) structures as indicated by different colors and labeled accordingly in Fig. 2. Structural details are provided in Appendix B.

For the sake of completeness, we further investigated the phase coexistence in our system: We have implemented the common tangent construction (Maxwell construction), i.e., we determine the convex hull of the energy curves for all considered structures. If the convex hull corresponds to the energy curve in a point, the respective structure is stable in that point. If the convex hull is a tangent connecting the energy curves of two structures, these two structures are in coexistence in that point, because a mixture of the respective structures possesses the smallest internal energy. That way we have determined the corresponding coexistence regimes between two neighboring phases, which we indicate by the yellow areas in the phase diagram in Fig. 2. As expected, the coexistence turns out to be relatively small at zero-temperature as compared to pure one-phase stability regimes.

The phases in Fig. 2 are shown for up to four particles per unit cell with solid colors. In addition, the regions where five or six particles per unit cell lead to new phases are marked by transparent colors encircled by the red lines. While outside of these regions we do not have any indication for the occurrence of phases with even more particles per unit cell, within the transparent regions more complex phases might be expected to be stable.

Our lattice-minimization routine reveals solely the stability of perfect lattices at zero-temperature. Having the possibility of stable nonperiodic structures in mind, we have included some quasicrystalline orderings according to the Penrose-, square-triangle-, and square-rhombic-tiling into our calculations by computing the potential energies per particle of large periodic approximants of the corresponding quasiperiodic tilings. As a result, within the studied parameter range, we have not observed any stable quasicrystalline phase.

C. Enthalpylike pair potential and occurrence of nontriangular phases

Obviously it would be of desire to predict where the nontrivial (i.e., the nontriangular) ground-state phases become stable just on a two-particle level without having to calculate the total energy of the system. While the densities where nontrivial phases in principle can occur might be roughly estimated from the pair potential, there is no direct way to predict whether there indeed is a nontrivial phase and where the onset in κd-direction of this phase is. Specifically, nontrivial phases can even occur for pair potentials that are strongly monotonic and for which it is not obvious why a ground state with multiple length scales should be stable. Of course, the reason for the occurrence of multiple length scales is the pressure that prevents the particles to just choose minima of the pair potential. In principle one could think of the pressure to force particles toward distances that are smaller than a possible minimum of the pair interaction potential corresponding to an effective tilt of this pair potential.

While the total area of the system is fixed, locally the area (or in three dimensions the volume) around particles, e.g., the area of Voronoi cells, can in principle vary from particle to particle. However, mechanical equilibrium requires that the pressure on the side of a Voronoi cell corresponds to the pressure on the neighboring cell. As a consequence, if one wants to break down a thermodynamic potential onto a two-particle level, the energy is not a good choice because the area is not fixed on the particle level. In contrast, the enthalpy is the thermodynamic potential that can be employed to predict ground states in case of fixed pressure (corresponding to results of other ensembles in the thermodynamic limits).

Therefore, we break down the enthalpy onto a two-particle level where the pressure is the same for different pairs of particles. The resulting enthalpylike pair potential on the two-particle level turns out to be a tilted pair interaction potential.

In the following we determine the two-particle enthalpylike quantity $h(r_{ij})$, where r_{ij} is the distance between the considered particles. This enthalpylike pair potential should be given such that its sums up to the total enthalpy H, i.e.,

$$H = \frac{1}{2}\sum_{i,j,i\neq j}^{N} h(r_{ij}) = U + pA, \tag{4}$$

where p is the macroscopic pressure and A the total area of the system (in three dimensions the volume has to be used instead). The enthalpylike pair potential therefore can be introduced as

$$h(r) = v(r) + 2\frac{p}{N}a(r), \tag{5}$$

where $a(r)$ is an effective surface area between any two particles at a relative distance r, which we refer to as the *pair area* in the following. The pair area $a(r)$ has to follow from a subdivision of the total area A as in

$$NA = \sum_{\substack{i,j\\ i\neq j}}^{N} a(r_{ij}). \tag{6}$$

Note that $a(r_{ij})$ shall be given such that for a fixed particle i, a summation over j leads to A. Then, a summation over all i and j with $i \neq j$ yields a total area of NA.

To get an idea what the enthalpylike pair potential can look like, we consider a particle i and its k neighbor shells. The remaining $N-1$ particles are distributed over these k shells. We denote the kth shell of i, to which the particle j belongs, by the index k_{ij}, its thickness by $\delta_{k_{ij}}$, its relative position to the particle i by $r_{k_{ij}}$, and the corresponding coordination number by $Z_{k_{ij}}$. Consequently, the pair area $a(r_{ij})$ can be written as the area of the kth shell of particle i to which the particle j belongs as

$$a(r_{ij}) \simeq \frac{2\pi}{Z_{k_{ij}}}\delta_{k_{ij}} r_{k_{ij}}, \tag{7}$$

where $1/Z_{k_{ij}}$ compensates the counting of multiple particles in the same shell so that each shell contributes only once to the sum in Eq. (6). While the coordination number can be easily obtained from the theta series of lattices, the most common ones of which being tabulated in Refs. [74,75], the choice of thickness δ_k is rather not trivial as the space can be subdivided differently into circular nonoverlapping rings under the constraint that each of which contain solely one neighbor shell. For the canonical choice of the thickness $\delta_k = (r_{k+1} - r_{k-1})/2$, where the shell positions r_k can be gained from the radial distribution function of the structure, we employ a polynomial fit up to the second order to the pair area from Eq. (7) over a range of the first six neighbor shells:

$$a(r) = B_1 + B_2\kappa r + B_3(\kappa r)^2, \tag{8}$$

with the distance r given in units of the screening length κ^{-1} and the coefficients B_1, B_2, and B_3 that depend on the depletion length and the density. In the considered range of r, the coefficient B_1 dominates over B_2 and B_3. Note that a subdivision of the total area A into pair areas $a(r)$ is not unique. However, as $a(r)$ is a function of the distance, we think that the use of concentric nonoverlapping shells for the pair areas is natural to obtain an approximation for $h(r)$, based on $h(r)$, and thus $a(r)$.

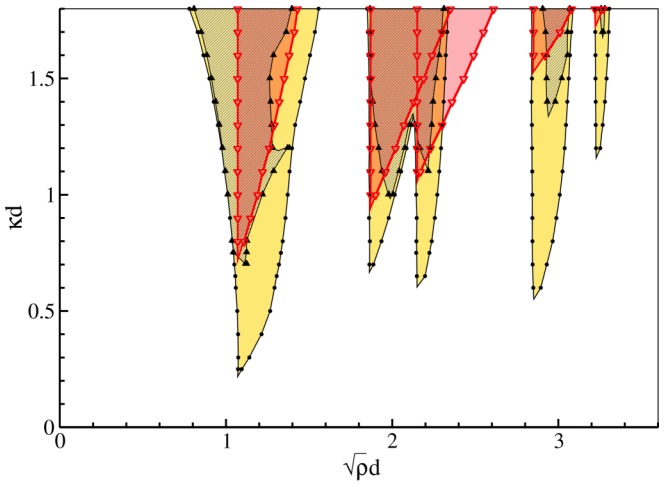

FIG. 3. Ground-state phase diagram of colloid-polymer mixtures. The majority of the phase space (white area) is governed by the triangular phase, whereas nontriangular phases can be stabilized around certain values of the reduced density and along the reduced depletion length. These nontriangular stability modes as determined by lattice-sum minimizations are shown by the yellow regions. The actual determined phase points at the boundary are indicated by the black dots. The red region indicates the theoretically predicted stability zone where complex nontriangular structures with two different length scales that are sufficiently distinct from the triangular length scale are expected to become stable. The hatched nontriangular subdomain comprises such stable complex phases as obtained by lattice-sum minimizations where the closest-neighbor distance in the first stability mode at $\sqrt{\rho}d \approx 1$ deviates at least 15% from the triangular lattice constant. Accordingly smaller thresholds are used for the hatched areas drawn in the higher nontriangular stability modes (yellow areas) at larger densities. The details are explained in the text.

If the enthalpy can be broken down into similar two-particle contributions as described above the following criteria for nontriangular phases has to hold: Complex nontriangular crystals with multiple length scales can occur as ground states if and only if there exists conditions at which the enthalpylike pair potential $h(r)$ possesses a concave region.

As shown in Fig. 3, the nontriangular crystalline phases only occur in special parameter regions that are marked in yellow for ground states as determined by minimizing the interaction energy. The red area indicates the phase space within which complex nontriangular structures are expected to become stable according to our enthalpy-based prediction. In the following, we explain our considerations and calculations to obtain the prediction shown in Fig. 3 for the system considered in this article in detail.

To predict where nontrivial phases at zero temperature can occur in the colloid-polymer mixture, we consider the explicit form of the pair interaction in Eq. (1), characteristic examples

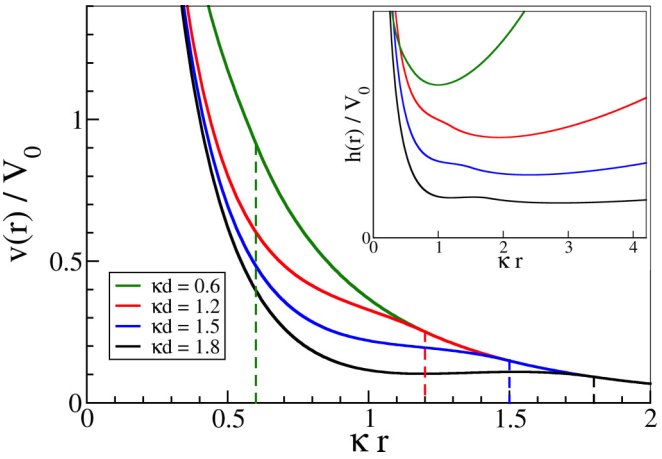

FIG. 4. Characteristic examples of pair interaction potentials $v(r)$ as given by Eq. (1). Potentials are shown for three different reduced depletion lengths ($\kappa d = 0.6, 1.2, 1.5, 1.8$), where the depletion lengths are indicated by the dashed lines. The inset illustrates the enthalpylike pair interaction h for $\kappa d = 0.6, 1.2, 1.5, 1.8$ at $\sqrt{\rho}d = 1.1$ as defined in Eq. (5), possessing a concave region for $\kappa d = 1.2, 1.5, 1.8$, and lacking such a region for $\kappa d = 0.6$, respectively. The same color code is used for both the main figure and the inset. We theoretically predict that whenever h exhibits a concave region, complex nontriangular phases are expected to become stable as shown by the red area in Fig. 3, and we support our predictions by rigorous numerical calculations of complex nontriangular phases as indicated by the hatched area in Fig. 3. Note that, in the inset, the enthalpylike pair interactions are arbitrarily shifted along the y axis for the sake of clarity.

of which are shown in Fig. 4 at different reduced depletion lengths κd and at $V_0/W_0 = 1$. For large $\kappa d = 1.8$, a single well occurs with a clear local maximum slightly below the reduced depletion length (the positions of which are indicated by dashed lines). We find that the nontriangular structures occur at reduced densities where the depletion length d approximately corresponds to the kth next-neighbor distance a_k of the triangular lattice with $k = 1, \cdots, 5$; cf. Fig. 3. These distances are a_1, $a_2 = \sqrt{3}a_1$, $a_3 = 2a_1$, $a_4 = \sqrt{7}a_1$, and $a_5 = 3a_1$ with $a_1 \approx 1/\sqrt{\rho}$. In other words; the triangular lattice is suppressed at densities where its interparticle distances roughly correspond to the depletion length of the system and thus being in the close vicinity of the maximum of the potential yielding an increase in the energy of the triangular lattice. The system will therefore possess lower potential energy for structurally more complex crystals with separated length scales or for rhombic or square lattice.

Note that nontriangular phases are still present at low reduced depletion lengths where the pair interaction potential does not possess a concave part, e.g., for $\kappa d = 0.6$ as shown by the green curve in Fig. 4. Recently developed inverse statistical-mechanical methods have been indeed used to engineer purely repulsive and convex interaction potentials that yield nontriangular ground-state crystals such as honeycomb lattice [28–32].

In the following, we analyze the conditions under which $h(r)$ might exhibit a concave region. Note that, unlike the pair interaction potential $v(r)$, the explicit form of $h(r)$ depends on the density via the macroscopic pressure p, cf. Eq. (5). The pressure p is given by $p = -\partial U/\partial A$ where in the vicinity of a given particle i we can use $dA_j = d(\pi r_{ij}^2) = 2\pi r_{ij} dr_{ij}$ as the change in the area and the energy per particle $u = U/N = \sum_{i,j,i\neq j} v(r_{ij})/2N \approx \sum_j v(r_{ij})$ for $T = 0$ such that $p/N \approx -\sum_j \frac{1}{2\pi r_{ij}} \partial v(r_{ij})/\partial r_{ij}$ in the ground state. At each density and depletion length, we obtain B_2 and B_3 from Eq. (8) and p/N for our reference system, i.e., the triangular lattice, and determine $h(r) = v(r) + 2p(B_2\kappa r + B_3\kappa^2 r^2)/N$. Note that B_1 in Eq. (8) represents an additive constant which when plugged into Eq. (5) does not change the qualitative form of $h(r)$.

In Fig. 3, the red area illustrates the phase space where h possesses a concave region and where in each nontriangular stability mode ($i = 1, \cdots, 5$, the yellow "fingers") the particles in the corresponding triangular shell k_i are located in this concave region. Within and only within this red area, we expect the stability of complex nontriangular phases if stability is dominated by the closer neighbors. If, however, the closest-neighbor distance in a nontriangular crystal deviates only slightly from the triangular lattice constant at the same density, it is then upon further neighbors whether the triangular or the nontriangular one becomes stable. For example, some regular phases like the square phase or rhombic phases that are morphologically close to the square phase are dominated by one nearest-neighbor length scale exactly as the triangular phase and therefore whether a triangular, a square or such a rhombic phase is stable not only depends on the closest neighbors. As a consequence, our theory can correctly predict a subdomain of the nontriangular stability region, and thus the red area shown in Fig. 3 differs from the nontriangular yellow area obtained by ground-state calculations, if, e.g., a square phase occurs.

Our approach captures the occurrence of some regular [e.g., elongated rhombic phases as shown in Fig. 6(b)] and complex phases (e.g., honeycomb, cluster phases, etc.) that are dominated by two nearest neighbors with distances sufficiently distinct from the triangular lattice constant. As an example; the hatched area in Fig. 3 indicates a subspace of nontriangular phases with stable complex phases whose nearest-neighbor distances differ at least 15% from the triangular lattice constant in the first, 7% in the second and third, and 3.5% in the fourth and fifth nontriangular stability modes. Note that the choice of such a distance cutoff is rather arbitrary. However, we observe the same qualitative picture for different cutoffs above 10% in the first nontriangular stability mode and accordingly adjusted cutoffs at larger stability modes. Moreover, we assumed so far that the triangular lattice is destabilized whenever its particles lie in the concave region of $h(r)$. This being a plausible assumption, we want to remark that the triangular order can also be suppressed when particle positions are slightly off the concave region due to subtle energy differences. We therefore anticipate minor broadening of the red area along the density axis at fixed κd when we slightly relax the sufficient condition, namely if we allow the triangular-lattice particles to be located close to but outside of the concave part of $h(r)$ to stabilize the complex nontriangular phases. Hence, the discrepancy between the red and the hatched area in Fig. 3 is not surprising.

So far we have investigated the phase diagrams of colloid-polymer mixtures at fixed $V_0/W_0 = 1$, where our theory—despite the aforementioned discrepancy—can predict remarkably well the occurrence of complex nontriangular phases. To convince the reader of the versatility of $h(r)$, we further studied the phase diagram in $(V_0/W_0, \sqrt{\rho}d)$ plane at fixed κd in Appendix C. Our enthalpy-based theory can not only capture the κd-values at which the complex nontriangular phases start to occur (cf. Fig. 3), it also correctly predicts the stability zone of complex nontriangular phases in $(V_0/W_0, \sqrt{\rho}d)$ plane, especially the V_0/W_0-values below which such complex structures become stable; see Fig. 13.

To demonstrate the explicit form of the enthalpy-like pair potential $h(r)$ in contrast to the pair potential $v(r)$, we plot $h(r)$ in the inset of Fig. 4 for $\kappa d = 0.6, 1.2, 1.5, 1.8$ with the reduced pressure $\tilde{p} \equiv 2pB_3/NV_0 \approx 0.61, 0.048, 0.019, 0.008$, respectively. These reduced pressure values are obtained at $\sqrt{\rho}d = 1.1$. Three of them, namely $\kappa d = 1.2, 1.5, 1.8$ show a clear concave region, whereas h for $\kappa d = 0.6$ lacks completely such a situation for any density. A comparison with Fig. 3 confirms our conjecture that if $h(r)$ has no concave region such as for $\kappa d = 0.6$, then we do not expect the stability of complex phases with multiple length scales that are fairly distinct from the triangular length scale.

The global order is still reflected by the pressure as well as the functional form $a(r)$ used to determine $h(r)$. As a consequence in principle $h(r)$ has to be determined for different candidate structures, to check whether the corresponding candidate structure minimizes the total enthalpy H as given in Eq. (4). However, since the functional form in Eq. (8) is a good approximation to many lattices, the enthalpylike function obtained by this choice for $a(r)$ can be used to check whether the triangular order is stable or not.

It is noteworthy that our criterion for nontriangular order does not take three-body or other higher multi-body interactions into account. Note that along the boundaries shown in Fig. 3 no triple overlaps of depletion zone occurs and therefore corrections due to many-body forces caused by multiple overlaps of diffusion zones do not affect these boundaries, while the boundaries between some of the complex phases shown in Fig. 2 in principle might change if many-body forces are considered.

To summarize the results of this subsection, by determining the enthalpylike pair potential $h(r)$ for triangular lattices we can predict the parameters where triangular order or other symmetries dominated by only one length scale can become unstable, namely if $h(r)$ possesses a concave part. Furthermore, we know that complex phases that are dominated by two distances between nearest neighbors can only occur if such a concave part exists. Note that instead of complex phase with two or more length scales in principle also a coexistence between phases with different length scales might occur.

IV. CONCLUSIONS

We have determined the ground-state phase diagram for a colloid polymer mixture, which we have modeled with effective pair interactions involving a short-ranged depletion attraction and a long-ranged screened electrostatic Coulomb repulsion. We have found a rich morphology: First, we identify large regions of triangular-lattice stability and regions of nontriangular lattices appearing as stability modes as a function of the density at fixed depletion length and polymer concentration. Second, the nontriangular regimes themselves feature a large diversity with respect to the stable phases. We recover simple phases such as rhombic and square lattices, but more interestingly, we also reveal complex phase structures with pentagon-, hexagon-, and octagon-based structures as well as trimers, triangle-rectangular and triangle-square crystals, most of which are also found to be stable at $T > 0$. Furthermore, some of these ground-state structures correspond to the well-known Archimedean tilings, self-assembly of which has attracted a special interest in fundamental and applied physical sciences [65–67].

Ground-state calculations can always depend on the candidate structures that are considered. We have determined all phases that are obtained for up to $n = 6$ particles per unit cell, where we show the phases for up to $n = 4$ particles per unit cell and indicate how an inclusion of $n = 5, 6$ particles into our minimization process yields slight changes shown by the transparent regions encircled by the red lines. The overall change when increasing the number of particles per unit cell is marginal and hence we only expect nonsignificant morphology changes of the nontriangular stability regions in the phase diagram in Fig. 2 upon an inclusion of $n > 6$ particles per unit cell. Our Brownian dynamics simulations confirm the triangular, square, rhombic, and pentagon-based structures. However, it is noteworthy that occurrence of exotic phases other than hitherto found ones within the stability zone of nontriangular lattices cannot be ultimately excluded.

In addition, we have developed a theoretical tool to predict the self-assembly of complex phase structures in classical condensed matter systems on a two-particle level. Our approach involves an enthalpylike pair potential. We found that our approach can identify the parameter region where complex structures with two or more length scales are stable.

By using Brownian dynamics simulations, we confirmed that the nontrivial phase regions observed in the ground state are still present at nonzero, small temperatures.

Our investigations have fundamental implications as we identified the ground-state phase diagram of colloid-polymer mixtures alongside a zoo of novel structures occurring in the same system, and practical implications as we establish systematic routes for the self-assembly of complex structures. These phases should be accessible in experiments and therefore our phase diagram explains how to tailor complex colloidal structures that might, e.g., be of interest for photonic applications: We observe that the nontriangular phases start to occur at $\kappa d \approx 1$, i.e., where the depletion length becomes approximately equal to the screening length. As a matter of fact, the screening length κ^{-1} can be tuned in experiments, e.g., by varying the salt concentration [76,77], and under ionized conditions, the screening length can be made notably smaller than the colloidal diameter. Consequently, the predicted complex phases can occur at depletion lengths smaller than the diameter. Note further that in experiments the depletion length can be as large as 1 μm, e.g., Ref. [78], and thus of the order of the particle diameter, while in many

systems it is smaller, i.e., $\kappa d > 1$; see Ref. [43]. Therefore, we expect that many experimental systems are in the parameter range where the predicted nontriangular phases can occur.

ACKNOWLEDGMENTS

We thank A. S. Kraemer, F. Martelli, and R. E. Rozas for illuminating discussions. E.C.O. and M.S. received financial support from the SFF of the HHU Düsseldorf. Furthermore, A.M. and M.S. were supported by the German Research Foundation (DFG) within the Emmy Noether program (Grant No. Schm 2657/2).

APPENDIX A: LATTICE-SUM MINIMIZATIONS

In the following we provide details of the lattice-sum minimizations employed to obtain the ground-state phase structures of colloid-polymer mixtures and the corresponding phase diagrams in Figs. 1, 2, and 3.

The system's behavior is dictated by the variables density ρ, inverse screening length κ, depletion length d, and energy amplitudes V_0 and W_0. Thus, for a given triplet of reduced parameters $(\sqrt{\rho}d, \kappa d, V_0/W_0)$, we find the stable phase at $T = 0$ by minimizing the corresponding potential-energy function per particle. As we restrict ourselves to periodic structures as possible candidates, we define the two-dimensional primitive cell to be a parallelogram with up to $n = 6$ particles and to be spanned by the two lattice vectors $\mathbf{a} = a(1, 0)$ and $\mathbf{b} = a\gamma(\cos\theta, \sin\theta)$, where γ denotes the aspect ratio ($\gamma = |\mathbf{b}|/|\mathbf{a}| = b/a$), and θ is the angle between $\mathbf{a}$ and $\mathbf{b}$, see Fig. 5. The position of a particle i in the parallelogram is specified by the vector $\mathbf{r}_i = (x_i, y_i)$. The total energy per particle can be written as $u = U/N = U_c/n$ with U_c denoting the *cell energy* given as

$$U_c = \frac{1}{2}\sum_{i,j=1}^{n}{\sum_{\mathbf{T}}}' v(|\mathbf{r}_i - \mathbf{r}_j + \mathbf{T}|), \tag{A1}$$

where v is the pair-interaction potential from Eq. (1), and $\mathbf{T} = l\mathbf{a} + m\mathbf{b}$ with $l, m \in \mathbb{N}$. The sum over $\mathbf{T}$ runs over all lattice cells where the prime indicates that for $\mathbf{T} = 0$ the terms with $i = j$ are omitted.

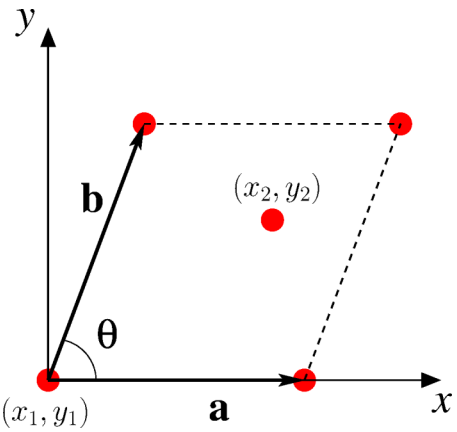

FIG. 5. Schematic illustration of a unit cell with two particles possessing spatial coordinates (x_i, y_i), $i = 1, 2$. The unit cell is a parallelogram spanned by the lattice vectors $\mathbf{a}$ and $\mathbf{b}$. In our numerical calculations, we minimize the angle θ between the lattice vectors, their aspect ratio $\gamma = |\mathbf{b}|/|\mathbf{a}|$, and the particle coordinates (x_i, y_i).

Given n particles in the cell, without loss of generality, we fix one particle at the origin such that we are left with $2(n - 1)$ positional parameters to minimize. We further include the geometrical parameters γ and θ into our minimization process to find the best possible cell shape. These parameters clearly set $\mathbf{b}$, and they dictate the lattice constant a via the density $\rho = n/|\mathbf{a} \times \mathbf{b}| = n/a^2\gamma \sin\theta$.

To deal with the infinite summation over $\mathbf{T}$ in Eq. (A1), i.e., summation over lattice cells using the integers l and m, we introduce a cutoff distance beyond which the additional energy gain is smaller than 10^{-8} times the total energy.

Lastly, we would like to mention that we have used the Nelder-Mead method [70] to minimize our lattice sums. Also known as downhill simplex or amoeba method, this method represents a gradient-free approach, and thus, it might converge faster than some conventional gradient-based algorithms. In recent years, more sophisticated optimization algorithms have been developed to improve the performance that make use of, e.g., evolutionary strategies [79,80]. This having said, however, we deal at most with $n = 6$ cell particles, i.e., 10 positional and 2 geometrical minimization parameters. Hence, for this small set of parameters at hand, we believe we do not need any highly sophisticated techniques to find the minimum-energy state. Importantly, we use up to 1000 independently and randomly generated start configurations of particle positions and cell shapes, where we observe already the final structure within 10–50 runs for up to $n = 4$, and within 50–200 for $n > 4$.

APPENDIX B: STRUCTURAL DETAILS OF STABLE PHASES

1. Triangular (Tr), rhombic (Rh), and square (Sq) phases

The ground-state phase diagram exhibits three simple crystalline phases, namely the triangular, rhombic, and square phases that are each shown in the left panels of Figs. 6(a)–6(c), respectively. The red lines serve as a guide to the eye showing the trivial unit cells in each structure. Characteristic snapshots of simple phases from finite-temperature BD simulations at $V_0/k_BT = 1000$ are displayed in the right panels of Figs. 6(a)–6(c).

We further identify plenty of complex structures containing at least two particles per unit cell. To achieve a clear overview for the reader, we choose to present them in groups according to the main repeating structural unit of each phase. Each group is uniquely color-coded in Fig. 2 as we use different colors and its shades for different groups. In the following, we list these groups alongside with structural images, and for clarity, we further regard the resulting structures as tilings, and we illustrate their prototiles.

2. Hexagon-based structures (Hex)

Hexagon-based structures appear in the first nontriangular region, albeit comprising regular hexagons as their main periodically repeating unit. For the sake of clarity, we provide a further point of view on the structures in the remainder of this paper: In addition to the unit cells that are marked red, we

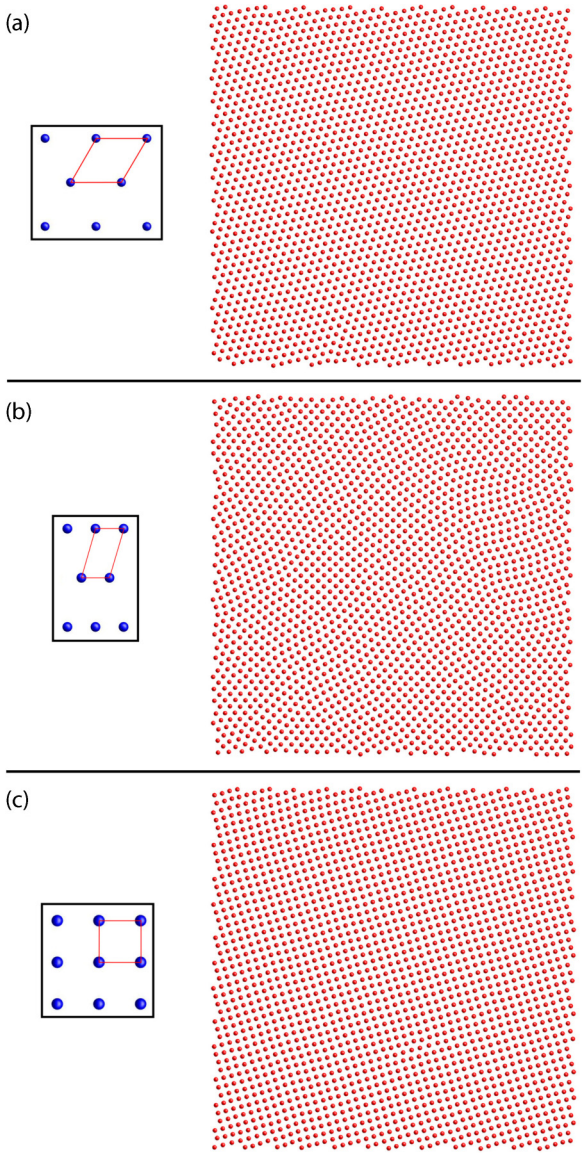

FIG. 6. Triangular (a), rhombic (b), and square (c) phases at $T = 0$ (left panels) as obtained by lattice-sum minimizations and $T > 0$ (right panels) as obtained by Brownian dynamics simulations. The red lines on the left panels depict the unit cells of the structures. The simulations contain $N = 2000$ particles.

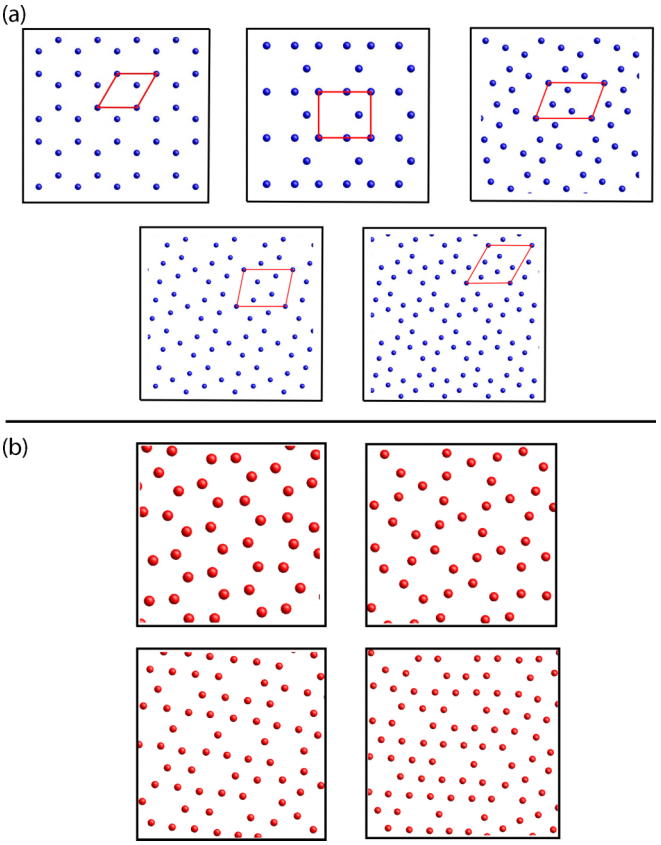

FIG. 7. Schematic illustration of five stable hexagon-based structures with regular hexagons as their main repeating units at $T = 0$ as obtained by lattice-sum minimizations (a), and finite patches of exemplary configurations with local hexagon formations at $T > 0$ as obtained from Brownian dynamics simulations (b). Different prototiles of the corresponding tilings are indicated by green lines in (a). These are either one hexagon or an hexagon with one or two different triangles. Note that the upper left structure corresponds to the honeycomb lattice. Red lines in (a) emphasize the unit cells with $n = 2, \ldots, 6$.

show the characteristic prototiles of the corresponding tilings by green lines in each figure. In this case, the prototiles are either a hexagon or a hexagon together with one or two distinct triangles as indicated by the green lines in Fig. 7(a). One of these structures corresponds to the well-known honeycomb lattice [upper left in Fig. 7(a)], whereas the other four consist of hexagons and triangles each in different stoichiometric ratios. This group is indicated by shades of green in Fig. 2 including the green transparent region with $n = 5, 6$. The latter are shown in the lower panel of Fig. 7(a).

The honeycomb lattice coincides with one of the three Platonic (regular) tilings, namely the hexagonal tiling, whereas the other two Platonic tilings are the trivial triangular and square ones which are obtained from the triangular and square lattice by connecting the nearest neighbors to each other to constitute the prototiles. The structure on the right hand side in the lower panel of Fig. 7(a) corresponds to one of the eight Archimedean tilings, namely to the so called *snub trihexagonal tiling*.

3. Octagon-based structures (Oct)

Octagon-based structures occur in the first nontriangular stability mode for $\kappa d > 1.5$ and $1.2 < \sqrt{\rho} d < 1.4$ and they are colored gray in Fig. 2 including the gray transparent region. We identify five different structures with a nonregular octagon as the main repeating unit, where four of them tile the space together with one or two different triangles (not necessarily equilateral). Hence, the prototiles are an octagon and one or two triangles as indicated by green lines in Fig. 8(a). The red lines show a minimal unit cell for each structure.

4. Trimers (Tri)

The trimer phase is found at $\kappa d > 1.7$ and $\sqrt{\rho} d \approx 0.9$ with the corresponding phase structures involving two

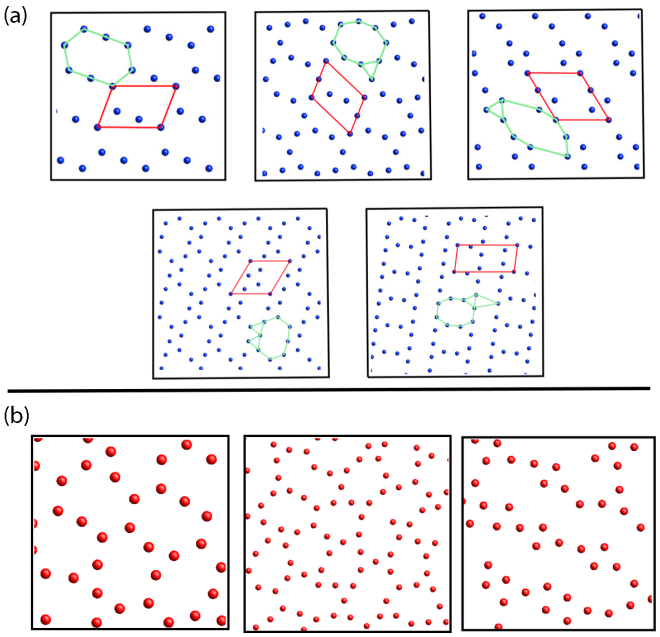

FIG. 8. Schematic illustration of five stable octagon-based structures with nonregular octagons as their main repeating units at $T = 0$ as obtained by lattice-sum minimizations (a), and finite patches of exemplary configurations with local octagon formations at $T > 0$ as obtained from Brownian dynamics simulations (b). The prototiles of the corresponding tilings are either one octagon or an octagon with one or two different triangles as indicated by green lines, whereas red lines mark the unit cells with $n = 3, 4, 5$ in (a).

well-separated length scales per dimension. The larger one dictates the periodicity of the overall lattice, whereas at the smaller length scale, the particles are arranged in equilateral triangles as a basis, see Fig. 9. The corresponding tiling possesses four distinct triangles as indicated by the green lines in the same figure, where also a unit cell with $n = 6$ is demonstrated by red lines.

Note that, in our finite-temperature simulations, we do not observe well-ordered trimers as shown in Fig. 9. We rather observe randomly distributed local trimer clusters without any orientational and translational long-ranged order. We have further noticed that in the vicinity of the zero-temperature

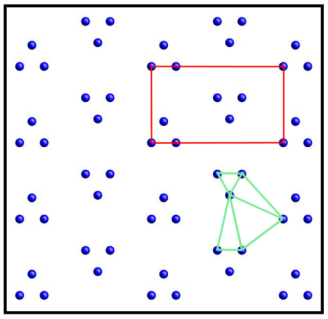

FIG. 9. Schematic illustration of a stable trimer structure at $T = 0$ as obtained by lattice-sum minimizations. The corresponding tiling can be constructed by four different triangles as its prototiles which are shown by green lines. Red lines mark the unit cell with $n = 6$.

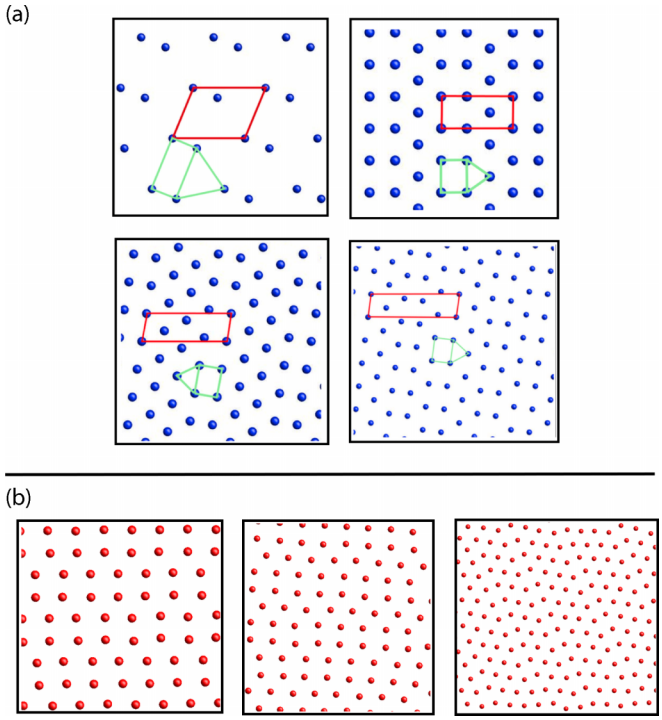

FIG. 10. Schematic illustration of four stable triangle-rectangular structures at $T = 0$ as obtained by lattice-sum minimizations (a), and finite patches of exemplary configurations with triangles and rectangles at $T > 0$ as obtained from Brownian dynamics simulations (b). The corresponding tiling has a rectangle and a triangle as its prototiles, whereas the ratio between them differs in each structure. Red lines in (a) mark the unit cells with $n = 2, \ldots, 5$.

density regime of trimers, our simulations also show dimers reminiscent of the upper left structure in Fig. 10(a) as will be discussed in the following.

5. Triangle-rectangular structures (TR)

Here, we reveal four different types of lattice structures, where we choose to demonstrate the lattice points as arranged in triangles and rectangles as basic constituents [prototiles of the corresponding tilings, cf. green lines in Fig. 10(a)]. Each structure possesses a different ratio between these constituents. The upper left structure of Fig. 10(a) occurs in the first nontriangular stability mode ($\sqrt{\rho}d < 1.1$), whereas the others are identified for $\kappa d > 1.3$ and $2.1 < \sqrt{\rho}d < 2.3$. The stability zones are shown by red areas in Fig. 2. As usual, the red lines in Fig. 10(a) depict the unit cells with $n = 2, \ldots, 5$.

6. Triangle-square structures (TS)

Triangle-square phase is indicated by the turquoise region in the phase diagram in Fig. 2 with the phase structure possessing four particles in the unit cell [cf. red lines in Fig. 11(a)]. The corresponding tiling consisting of equilateral triangles and squares as specified by the green lines in Fig. 11(a) is revealed to be the *snub square* tiling, also known as σ- or H-phase, which corresponds to one of the eight Archimedean tilings.

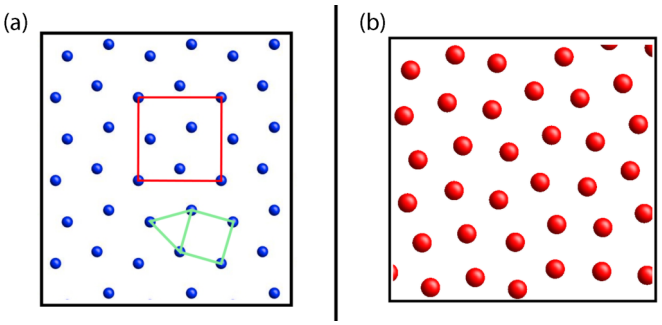

FIG. 11. Schematic illustration of a stable triangle-square structure at $T = 0$ as obtained by lattice-sum minimizations (a), and a finite patch of an exemplary configuration with triangle-square formation at $T > 0$ as obtained from Brownian dynamics simulations (b). It composes of a square and a triangle as the prototiles of the corresponding tiling. Red lines in a) mark the unit cell with $n = 4$.

7. Pentagon-based structures (Pen)

In this group, we have four perfect ground-state lattice structures possessing $n = 5$ ($n = 6$) as shown in the upper (lower) level of Fig. 12(a), with the red lines indicating the corresponding unit cells. These structures are found in a relatively broad regime in the first nontriangular stability mode for $1.1 < \sqrt{\rho}d < 1.4$ around $\kappa \approx 1$ as well as in a tiny regime for $\sqrt{\rho}d \approx 2.15$ and $\kappa d > 1.7$. These regions are indicated by the purple transparent areas in Fig. 2.

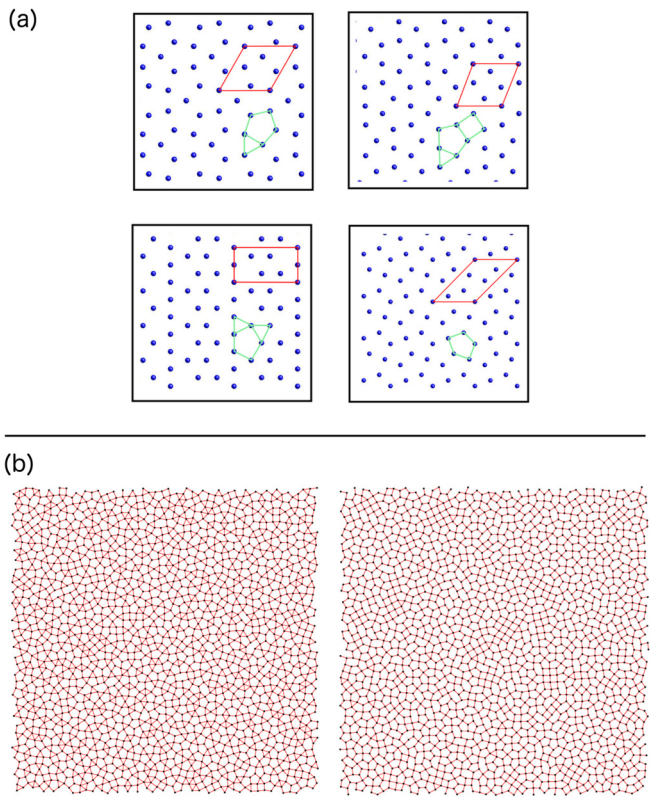

FIG. 12. Stable pentagon-based structures at (a) $T = 0$ as obtained by lattice-sum minimizations and (b) $T > 0$ with nonregular pentagons being the main repeating unit as obtained by Brownian dynamics simulations. The four crystalline ground-state structures are schematically illustrated in (a), where green lines indicate the different prototiles of the corresponding tilings, and red lines emphasize the unit cell in each structure. In (b), two characteristic simulation snapshots are shown exhibiting high local pentagonal order and resembling some of the pentagon-based structures from (a).

As seen in Fig. 12(a), the pentagon-based structures differ in the type and number of prototiles, that is, some of them tile the space periodically by just one nonregular pentagon, whereas others need (beside the pentagon) one or two different triangles or a triangle and a square.

In Fig. 12(b), we demonstrate two characteristic snapshots of finite-temperature simulations showing clear local pentagonal orderings. Black dots represent particle positions, whereas red lines have been introduced to connect the nearest neighbors based on a distance criterion, and thus to highlight a possible tessellation of the space with pentagons. The basic difference between both snapshots in Fig. 12(b) is that the left one comprises predominantly pentagons and rhombuses as tiles, whereas in the right image there exists a considerable amount of triangles beside the pentagons, suggesting a strong resemblance to the ground-state structure shown on the upper left in Fig. 12(a). We would like to mention that we have undertaken different runs starting from random, triangular, and square lattice configurations, and all runs lead to very similar final configurations displaying the same local pentagonal orderings at prescribed system parameters.

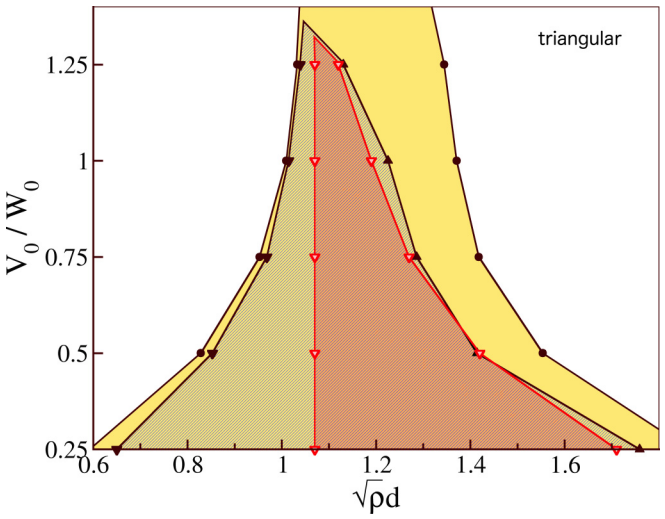

FIG. 13. Ground-state phase diagram of colloid-polymer mixtures at fixed $\kappa d = 1$. The nontriangular stability mode as determined by lattice-sum minimizations is shown by the yellow region. The actual determined phase points at the boundary are indicated by the corresponding tokens. The red region indicates the theoretically predicted stability zone where complex nontriangular structures with two different length scales that are sufficiently distinct from the triangular length scale are expected to become stable. The hatched nontriangular subdomain comprises such stable complex phases as obtained by lattice-sum minimizations where the closest-neighbor distance deviates at least fifteen percent from the triangular lattice constant.

APPENDIX C: PHASE DIAGRAM IN $(V_0/W_0, \sqrt{\rho}d)$-PLANE

In Fig. 13 we present the phase diagram as a function of the ratio of the energy amplitudes $0.25 < V_0/W_0 < 1.4$ and the reduced density $0.6 < \sqrt{\rho}d < 1.8$ at fixed $\kappa d = 1$, focusing thereby on the first nontriangular stability mode. The yellow area indicates as usual the nontriangular phases as determined by lattice-sum minimizations, whereas the red area shows the theoretical prediction of the complex phases based on $h(r)$. Our theoretical approach is able to capture quite well the stability of complex phases whose next-neighbour distances deviates at least 15% from the triangular lattice constant at the respective density (cf. the hatched area).

[1] G. M. Whitesides, J. P. Mathias, and C. T. Seto, Molecular self-assembly and nanochemistry: A chemical strategy for the synthesis of nanostructures, Science **254**, 1312 (1991).

[2] G. M. Whitesides and B. Grzybowski, Self-assembly at all scales, Science **295**, 2418 (2002).

[3] G. M. Whitesides and M. Boncheva, Beyond molecules: Self-assembly of mesoscopic and macroscopic components, Proc. Natl. Acad. Sci. U.S.A. **99**, 4769 (2002).

[4] R. Groß and M. Dorigo, Self-assembly at the macroscopic scale, Proc. IEEE **96**, 1490 (2008).

[5] J.-M. Lehn, Toward self-organization and complex matter, Science **295**, 2400 (2002).

[6] S. A. Jenekhe and X. L. Chen, Self-assembly of ordered microporous materials from rod-coil block copolymers, Science **283**, 372 (1999).

[7] A. M. Jackson, J. W. Myerson, and F. Stellacci, Spontaneous assembly of subnanometre-ordered domains in the ligand shell of monolayer-protected nanoparticles, Nat. Mater. **3**, 330 (2004).

[8] V. N. Manoharan, M. T. Elsesser, and D. J. Pine, Dense packing and symmetry in small clusters of microspheres, Science **301**, 483 (2003).

[9] W. M. Jacobs and D. Frenkel, Self-assembly of structures with addressable complexity, J. Am. Chem. Soc. **138**, 2457 (2016).

[10] D. J. Kushner, Self-assembly of biological structures, Bacteriological Reviews **33**, 302 (1969).

[11] Y. Engelborghs, Microtubules: Dissipative structures formed by self-assembly, Biosensors & Bioelectronics **9**, 685 (1994).

[12] E. O. Budrene and H. C. Berg, Dynamics of formation of symmetrical patterns by chemotactic bacteria, Nature **376**, 49 (1995).

[13] J. D. Halley and D. A. Winkler, Critical-like self-organization and natural selection: Two facets of a single evolutionary process? BioSystems **92**, 148 (2008).

[14] T. Dotera, T. Oshiro, and P. Ziherl, Mosaic two-lengthscale quasicrystals, Nature **506**, 208 (2014).

[15] D. Shechtman, I. Blech, D. Gratias, and J. W. Cahn, Metallic Phase with Long Range Orientational Order and no Translation Symmetry, Phys. Rev. Lett. **53**, 1951 (1984).

[16] L. Assoud, R. Messina, and H. Löwen, Stable crystalline lattices in two-dimensional binary mixtures, Eur. Phys. Lett. **80**, 48001 (2007).

[17] L. Assoud, R. Messina, and H. Löwen, Binary crystals in two-dimensional two-component yukawa mixtures, J. Chem. Phys. **129**, 164511 (2008).

[18] M. Antlanger and G. Kahl, Wigner crystals for a planar, equimolar binary mixture of classical, charged particles, Condens. Matter Phys. **16**, 43501 (2013).

[19] P. F. Damasceno, M. Engel, and S. C. Glotzer, Predictive self-assembly of polyhedra into complex structures, Science **337**, 453 (2012).

[20] Q. Chen, S. C. Bae, and S. Granick, Directed self-assembly of a colloidal Kagome lattice, Nature **469**, 381 (2011).

[21] G. Doppelbauer, E. G. Noya, E. Bianchi, and G. Kahl, Self-assembly scenarios of patchy colloidal particles, Soft Matter **8**, 7768 (2012).

[22] E. Bianchi, C. N. Likos, and G. Kahl, Tunable assembly of heterogeneously charged colloids, Nano Lett. **14**, 3412 (2014).

[23] M. Rechtsman, F. H. Stillinger, and S. Torquato, Optimized Interactions for Targeted Self-Assembly: Application to a Honeycomb Lattice, Phys. Rev. Lett. **95**, 228301 (2005).

[24] M. Rechtsman, F. H. Stillinger, and S. Torquato, Designed interaction potentials via inverse methods for self-assembly, Phys. Rev. E **73**, 011406 (2006).

[25] R. D. Batten, F. H. Stillinger, and S. Torquato, Classical disordered ground states: Super-ideal gases and stealth and equiluminous materials, J. Appl. Phys. **104**, 033504 (2008).

[26] S. Torquato, Inverse optimization techniques for targeted self-assembly, Soft Matter **5**, 1157 (2009).

[27] H. Cohn and A. Kumar, Algorithmic design of self-assembling structures, Proc. Natl. Acad. Sci. U.S.A. **106**, 9570 (2009).

[28] É. Marcotte, F. H. Stillinger, and S. Torquato, Unusual ground states via monotonic convex pair potentials, J. Chem. Phys. **134**, 164105 (2011).

[29] A. Jain, J. R. Errington, and T. M. Truskett, Inverse design of simple pairwise interactions with low coordinated 3D lattice ground states, Soft Matter **9**, 3866 (2013).

[30] A. Jain, J. R. Errington, and T. M. Truskett, Dimensionality and Design of Isotropic Interactions That Stabilize Honeycomb, Square, Simple Cubic, and Diamond Lattices, Phys. Rev. X **4**, 031049 (2014).

[31] W. D. Piñeros, M. Baldea, and T. M. Truskett, Designing convex repulsive pair potentials that favor assembly of Kagome and snub square lattices, J. Chem. Phys. **145**, 054901 (2016).

[32] W. D. Piñeros, M. Baldea, and T. M. Truskett, Breadth versus depth: Interactions that stabilize particle assemblies to changes in density or temperature, J. Chem. Phys. **144**, 084502 (2016).

[33] A. A. Louis, Beware of density dependent pair potentials, J. Phys.: Condens. Matter **14**, 9187 (2002).

[34] R. Castañeda-Priego, A. Rodríguez-López, and J. M. Méndez-Alcaraz, Depletion forces in two-dimensional colloidal mixtures, J. Phys.: Condens. Matter **15**, S3393 (2003).

[35] P. Domínguez-García, Microrheological consequences of attractive colloid-colloid potentials in a two-dimensional brownian fluid, Eur. Phys. J. E **35**, 73 (2012).

[36] L. Feng, B. Laderman, S. Sacanna, and P. Chaikin, Re–entrant solidification in polymer-colloid mixtures as a consequence of competing entropic and enthalpic attractions, Nat. Mater. **14**, 61 (2015).

[37] K. N. Pham, A. M. Puertas, J. Bergenholtz, S. U. Egelhaaf, A. Moussaid, P. N. Pusey, A. B. Schofield, M. E. Cates, M. Fuchs,

and W. C. K. Poon, Multiple glassy states in a simple model system, Science **296**, 104 (2002).
[38] T. Eckert and E. Bartsch, Re-Entrant Glass Transition in a Colloid-Polymer Mixture with Depletion Attractions, Phys. Rev. Lett. **89**, 125701 (2002).
[39] S. Manley, H. M. Wyss, K. Miyazaki, J. C. Conrad, V. Trappe, L. J. Kaufman, D. R. Reichman, and D. A. Weitz, Glasslike Arrest in Spinodal Decomposition as a Route to Colloidal Gelation, Phys. Rev. Lett. **95**, 238302 (2005).
[40] P. J. Lu, E. Zaccarelli, F. Ciulla, A. B. Schofield, F. Sciortino, and D. A. Weitz, Gelation of particles with short-range attraction, Nature **453**, 499 (2008).
[41] I. Zhang, C. P. Royall, M. A. Faers, and P. Bartlett, Phase separation dynamics in colloid-polymer mixtures: The effect of interaction range, Soft Matter **9**, 2076 (2013).
[42] Ethayaraja Mani, Wolfgang Lechner, Willem K. Kegel, and Peter G. Bolhuis, Equilibrium and nonequilibrium cluster phases in colloids with competing interactions, Soft Matter **10**, 4479 (2014).
[43] M. Kohl, R. F. Capellmann, M. Laurati, S. U. Egelhaaf, and M. Schmiedeberg, Directed percolation identified as equilibrium pre–transition towards non-equilibrium arrested gel states, Nat. Commun. **7**, 11817 (2016).
[44] A. Stradner, H. Sedgwick, F. Cardinaux, W. C. K. Poon, S. U. Egelhaaf, and P. Schurtenberger, Equilibrium cluster formation in concentrated protein solutions and colloids, Nature **432**, 492 (2004).
[45] J. Taffs, A. Malins, S. R. Williams, and C. P. Royall, A structural comparison of models of colloid-polymer mixtures, J. Phys.: Condens. Matter **22**, 104119 (2010).
[46] F. Leal Calderon, J. Bibette, and J. Biais, Experimental phase diagrams of polymer and colloid mixtures, Europhys. Lett. **23**, 653 (1993).
[47] M. Dijkstra, R. van Roij, and R. Evans, Phase diagram of highly asymmetric binary hard-sphere mixtures, Phys. Rev. E **59**, 5744 (1999).
[48] J.-T. Lee and M. Robert, Phase transitions of colloid-polymer systems in two dimensions, Phys. Rev. E **60**, 7198 (1999).
[49] M. Schmidt, H. Löwen, J. M. Brader, and R. Evans, Density functional theory for a model colloid–polymer mixture: Bulk fluid phases, J. Phys.: Condens. Matter **14**, 9353 (2002).
[50] W. C. K. Poon, The physics of a model colloid–polymer mixture, J. Phys.: Condens. Matter **14**, R859 (2002).
[51] D. G. A. L. Aarts, R. Tuinier, and H. N. W. Lekkerkerker, Phase behavior of mixtures of colloidal spheres and excluded-volume polymer chains, J. Phys.: Condens. Matter **14**, 7551 (2002).
[52] C. P. Royall, D. G. A. L. Aarts, and H. Tanaka, Fluid structure in colloid-polymer mixtures: The competition between electrostatics and depletion, J. Phys.: Condens. Matter **17**, S3401 (2005).
[53] A. Fortini, M. Dijkstra, and R. Tuinier, Phase behavior of charged colloidal sphere dispersions with added polymer chains, J. Phys.: Condens. Matter **17**, 7783 (2005).
[54] Gerard J. Fleer and Remco Tuinier, Analytical phase diagram for colloid-polymer mixtures, Phys. Rev. E **76**, 041802 (2007).
[55] Gerard J. Fleer and Remco Tuinier, Analytical phase diagrams for colloids and nonadsorbing polymer, Adv. Colloid Interface Sci. **143**, 1 (2008).
[56] R. Tuinier, P. A. Smith, W. C. K. Poon, S. U. Egelhaaf, D. G. A. L. Aarts, H. N. W. Lekkerkerker, and G. J. Fleer, Phase diagram for a mixture of colloids and polymers with equal size, Europhys. Lett. **82**, 68002 (2008).
[57] Á. González García and R. Tuinier, Tuning the phase diagram of colloid-polymer mixtures via yukawa interactions, Phys. Rev. E **94**, 062607 (2016).
[58] A. Moncho-Jordá, A. A. Loius, P. G. Bolhuis, and R. Roth, The Asakura-Oosawa model in the protein limit: The role of many-body interactions, J. Phys.: Condens. Matter **15**, S3429 (2003).
[59] M. Dijkstra, R. van Roij, R. Roth, and A. Fortini, Effect of many-body interactions on the bulk and interfacial phase behavior of a model colloid-polymer mixture, Phys. Rev. E **73**, 041404 (2006).
[60] B. Cui, B. Lin, D. Frydel, and S. A. Rice, Anomalous behavior of the depletion potential in quasi-two-dimensional binary mixtures, Phys. Rev. E **72**, 021402 (2005).
[61] D. Frydel and S. A. Rice, Depletion interaction in a quasi-two-dimensional colloid assembly, Phys. Rev. E **71**, 041402 (2005).
[62] A. Fortini, M. Schmidt, and M. Dijkstra, Phase behavior and structure of model colloid-polymer mixtures confined between two parallel planar walls, Phys. Rev. E **73**, 051502 (2006).
[63] R. L. C. Vink, K. Binder, and J. Horbach, Critical behavior of a colloid-polymer mixture confined between walls, Phys. Rev. E **73**, 056118 (2006).
[64] J. Kepler, *Harmonices Mundi* (Linz, Austria, 1619).
[65] M. Schmiedeberg, J. Mikhael, S. Rausch, J. Roth, L. Helden, C. Bechinger, and H. Stark, Archimedean-like colloidal tilings on substrates with decagonal and tetradecagonal symmetry, Eur. Phys. J. E **32**, 25 (2010).
[66] M. Antlanger, G. Doppelbauer, and G. Kahl, On the stability of archimedean tilings formed by patchy particles, J. Phys.: Condens. Matter **23**, 404206 (2011).
[67] J. A. Millan, D. Ortiz, G. van Anders, and S. C. Glotzer, Self-assembly of archimedean tilings with enthalpically and entropically patchy polygons, ACS Nano **8**, 2918 (2014).
[68] S. Asakura and F. Oosawa, On interaction between two bodies immersed in a solution of macromolecules, J. Chem. Phys. **22**, 1255 (1954).
[69] A. Vrij, Polymers at interfaces and interactions in colloidal dispersions, Pure Appl. Chem. **48**, 471 (1976).
[70] J. A. Nelder and R. A. Mead, A simplex method for function minimization, Comput. J. **7**, 308 (1965).
[71] J. de Graaf, L. Filion, M. Marechal, R. van Roij, and M. Dijkstra, Crystal-structure prediction via the floppy-box Monte Carlo algorithm: Method and application to hard (non)convex particles, J. Chem. Phys. **137**, 214101 (2012).
[72] A.-P. Hynninen and M. Dijkstra, Phase diagram of hard-core repulsive yukawa particles with a density-dependent truncation: A simple model for charged colloids, J. Phys.: Condens. Matter **15**, S3557 (2003).
[73] M. O. Robbins, K. Kremer, and G. S. Grest, Phase diagram and dynamics of Yukawa systems, J. Chem. Phys. **88**, 3286 (1988).
[74] N. J. A. Sloane, Theta series and magic numbers for diamond and certain ionic crystal structures, J. Math. Phys. **28**, 1653 (1987).
[75] J. H. Conway and N. J. A. Sloane, *Sphere Packings, Lattices and Groups*, 3rd ed. (Springer, New York, 1999).
[76] E. C. Oğuz, A. Reinmüller, H. J. Schöpe, T. Palberg, R. Messina, and H. Löwen, Crystalline multilayers of charged

colloids in soft confinement: Experiment versus theory, J. Phys.: Condens. Matter **24**, 464123 (2012).

[77] A. Yethiraj and A. Blaaderen, A colloidal model system with an interaction tunable from hard sphere to soft and dipolar, Nature **421**, 513 (2003).

[78] C. P. Royall, M. E. Leunissen, A.-P. Hynninen, M. Dijkstra, and A. van Blaaderen, Re-entrant melting and freezing in a model system of charged colloids, J. Chem. Phys. **124**, 244706 (2006).

[79] I. Loshchilov, T. Glasmachers, and H.-G. Beyer, Large scale black-box optimization by limited-memory matrix adaptation, IEEE Trans. Evol. Comput. (to be published)..

[80] D. Wilson, S. Rodrigues, C. Segura, I. Loshchilov, F. Hutter, G. L. Buenfil, A. Kheiri, E. Keedwell, M. Ocampo-Pineda, E. Özcan, S. I. V. Peña, B. Goldman, S. B. Rionda, A. Hernández-Aguirre, K. Veeramachaneni, and S. Cussat-Blanc, Evolutionary computation for wind farm layout optimization, Renew. Energy **126**, 681 (2018).